ACS central science

http://pubs.acs.org/journal/acscii

Research Article

Probing Kinetics of Water-in-Salt Aqueous Batteries with Thick Porous Electrodes

Cheng-Hung Lin, Lei Wang, Steven T. King, Jianming Bai, Lisa M. Housel, Alison H. McCarthy, Mallory N. Vila, Hengwei Zhu, Chonghang Zhao, Lijie Zou, Sanjit Ghose, Xianghui Xiao, Wah-Keat Lee, Kenneth J. Takeuchi, Amy C. Marschilok, Esther S. Takeuchi, Mingyuan Ge,* and Yu-chen Karen Chen-Wiegart*

Cite This: https://doi.org/10.1021/acscentsci.1c00878

Read Online

ACCESS | Metrics & More | Article Recommendations | Supporting Information

ABSTRACT: Aqueous electrochemical systems suffer from a low energy density due to a small voltage window of water (1.23 V). Using thicker electrodes to increase the energy density and highly concentrated "water-in-salt" (WIS) electrolytes to extend the voltage range can be a promising solution. However, thicker electrodes produce longer diffusion pathways across the electrode. The highly concentrated salts in WIS electrolytes alter the physicochemical properties which determine the transport behaviors of electrolytes. Understanding how these factors interplay to drive complex transport phenomena in WIS batteries with thick electrodes via deterministic analysis on the rate-limiting factors and kinetics is critical to enhance the rate-performance in these batteries. In this work, a multimodal approach—Raman tomography, *operando* X-ray diffraction refinement, and synchrotron X-ray 3D spectroscopic imaging—was used to investigate the chemical heterogeneity in LiV_3O_8–$LiMn_2O_4$ WIS batteries with thick porous electrodes cycled under different rates. The multimodal results indicate that the ionic diffusion in the electrolyte is the primary rate-limiting factor. This study highlights the importance of fundamentally understanding the electrochemically coupled transport phenomena in determining the rate-limiting factor of thick porous WIS batteries, thus leading to a design strategy for 3D morphology of thick electrodes for high-rate-performance aqueous batteries.

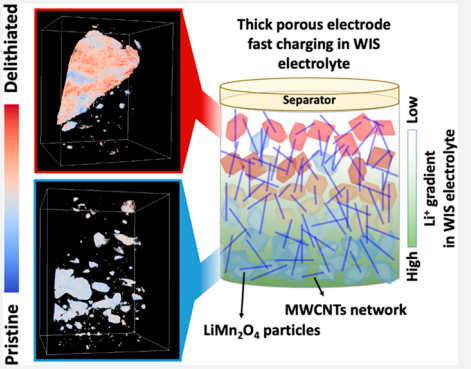

INTRODUCTION

Extending applications of energy storage from electronic devices to electrical vehicles and grid storage pushes battery technologies, such as Li-ion and beyond-Li systems, to demand higher energy density, better safety, lower environmental impact, and lower cost.[1,2] Concerns of safety and environmental impacts mainly come from the usage of organic solvents as electrolytes which demonstrate an outstanding electrochemical performance in current Li-ion batteries but are highly flammable.[3−5] Li-ion batteries and beyond-Li systems based on aqueous electrolytes could be a solution to resolve these concerns by reducing the risk of fire, toxicity, and the cost to maintain a rigorous manufacturing environment.[5−7] Despite the benefits of aqueous Li-ion batteries, aqueous electrolytes exhibit lower electrolyte stability because of the limited voltage window of water (∼1.23 V), leading to unsatisfactory energy density and capacity retention.[8−10] Research efforts have been dedicated to increasing the operating voltage, energy density, and capacity retention; aqueous batteries with stable cycling at ∼1.5 V through arranging electrode materials and tuning the pH values of electrolytes have been reported.[10−12] In the family of aqueous electrolytes, water-in-salt (WIS) electrolytes, through dissolving ultrahigh concentrations of salts in water, effectively increase the voltage window of electrolyte (>3.0 V which depends on salt components and concentrations) and thus hold a promising direction for future aqueous batteries.[13−17]

However, due to the ultrahigh concentration, the physicochemical properties of WIS electrolytes, such as density, viscosity, diffusivity, and ionic conductivity, exhibit an apparent deviation from conventional dilute electrolytes, as summarized in Table S1.[15,17−21] This deviation alters the transport phenomena in electrochemistry and leads to complex transport behaviors. Some recent works simulating the transport properties in WIS electrolytes showed that the anions in a WIS system can form a percolating network resulting in a larger Li^+ transport or transference number than conventional electrolytes, while the overall diffusivities of all species decreased as electrolyte concentration increased.[19,21−23] Despite the contribution of

Received: July 20, 2021

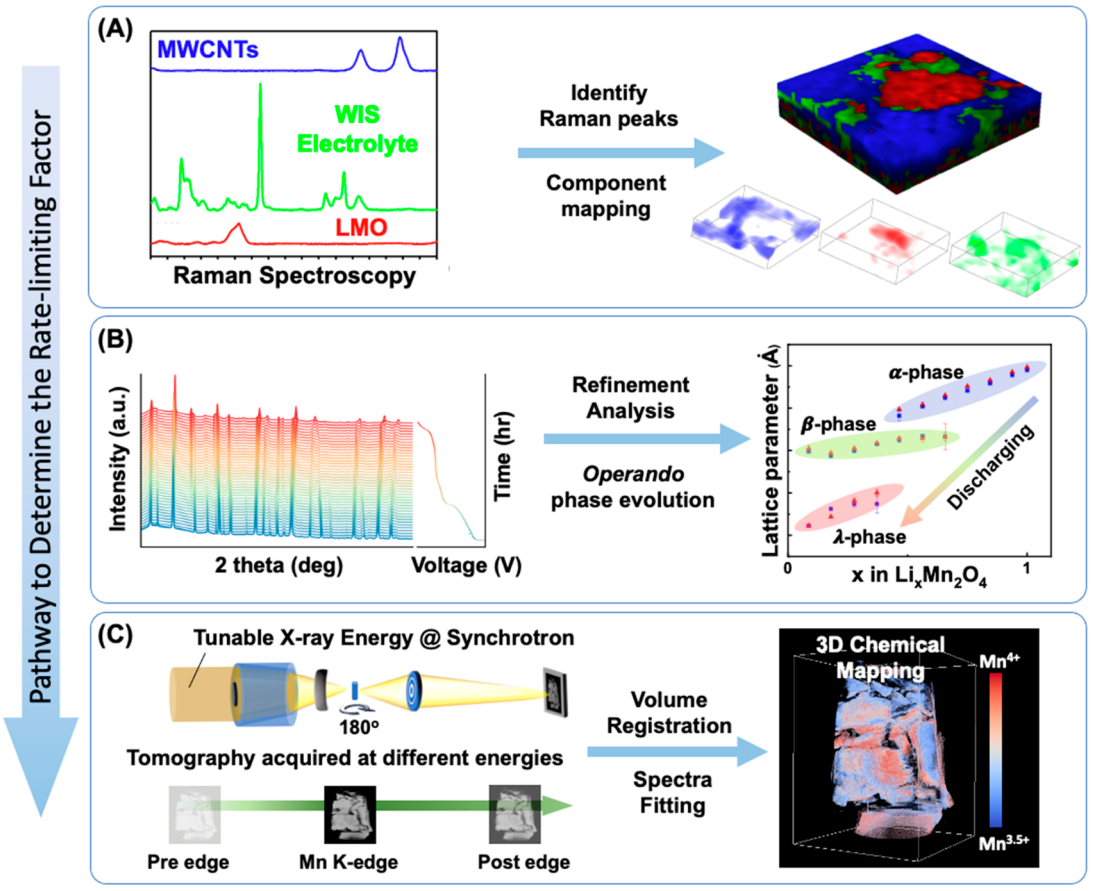

Figure 1. Research concept and experimental setup for the kinetics study of thick porous LiV_3O_8−$LiMn_2O_4$ aqueous Li-ion batteries. (A) Raman mapping of MWCNTs, WIS electrolyte, and LMO to identify the electrolyte pathway in thick porous LMO electrodes. (B) *Operando* X-ray diffraction to quantify the phase evolution by peak profile fitting and Rietveld refinement. (C) 3D XANES tomography to map the spatial chemical heterogeneity.

the simulations, the transport kinetics becomes further convoluted, while another solution to increase the energy density from the engineering aspect is introduced to build a thick architecture electrode.[24] The increased thickness in thick electrodes significantly elongates the conductive pathway required of electrons across the electrode and the ionic diffusion length in the electrolyte within the electrodes' pores.[25−27] These longer transport pathways result in increased cell polarization and lower active material utilization in nonaqueous batteries,[28] as well as compromised rate performance.[25,29−31]

Furthermore, for the same active materials (thus the same ionic diffusivity in the solid phase), the electron and ionic transport properties of the porous electrode are directly impacted by the 3D morphology of electrode as well as the intrinsic ionic diffusivity (in the electrolyte) and the electron conductivity (in the electrode). For instance, when considering the ionic diffusion in porous battery electrodes, this leads to a reduction of the effective diffusion coefficient by $D_{\text{eff}} = D\frac{\varepsilon}{\tau^2}$, where D is the intrinsic diffusion coefficient in a nontortuous path, ε is the porosity, and τ is the tortuosity of the structure;[32,33] the conductivity also follows a similar relationship.[34] Note that the tortuosity and porosity are not independent and can often be correlated by the Bruggeman relation ($\tau^2 = \varepsilon^{1-\alpha}$, where α is the Bruggeman coefficient)[35] or its derivations, depending on the geometry. Here, the intrinsic diffusion coefficient D is a function of the electrolyte concentration. In general, the ionic diffusivity in the concentrated electrolyte can be correlated with the viscosity by the Stokes−Einstein relation: $D{\cdot}\eta = kT/6\pi r$, or $\mu{\cdot}\eta = q/6\pi r$, where D is the diffusivity, and μ is the mobility of an ion and can be expressed in terms of diffusivity ($\mu = \frac{q}{kT}D$), k is the Boltzmann constant, T is the absolute temperature, η is the viscosity of the electrolyte, r is the radius of the solute molecule, and q is the charge of an ion.[36] Note that the Stokes−Einstein relation applies to ideal solutions, while a revised form ($D{\cdot}\eta^{\beta}/T$ = constant) needs to be considered in highly concentrated solutions due to the diffusion−viscosity decoupling effect, where β is the decoupling factor and smaller than 1.[15,19,21] These relations show that the effective diffusion coefficient strongly depends on the electrolyte properties and electrode geometry. As a result, unveiling the kinetic limitations is required, while the transport phenomena in WIS electrolyte and thick electrodes with different 3D morphological factors are convoluted. In particular, kinetically suppressing hydrogen evolution and formation of a stable solid electrolyte interface (SEI) layer in WIS batteries are more efficient at high rates.[37−40] Such knowledge is necessary to design an aqueous battery for fast charge−discharge and high energy density applications.

In this work, the rate-limiting factor in a WIS battery with thick porous electrodes is revealed through a multimodal analysis—Raman tomography, *operando* X-ray diffraction refinement, and synchrotron X-ray 3D spectroscopic imaging. An electrode couple with LiV_3O_8 (LVO) as the anode and $LiMn_2O_4$ (LMO) as the cathode was selected to be studied in a bisalt WIS electrolyte with various electrode thicknesses and porosities. The bisalt WIS electrolyte is composed of lithium bis(trifluoromethanesulfonyl)imide (LiTFSI) and lithium bis-

https://doi.org/10.1021/acscentsci.1c00878
ACS Cent. Sci. XXXX, XXX, XXX−XXX

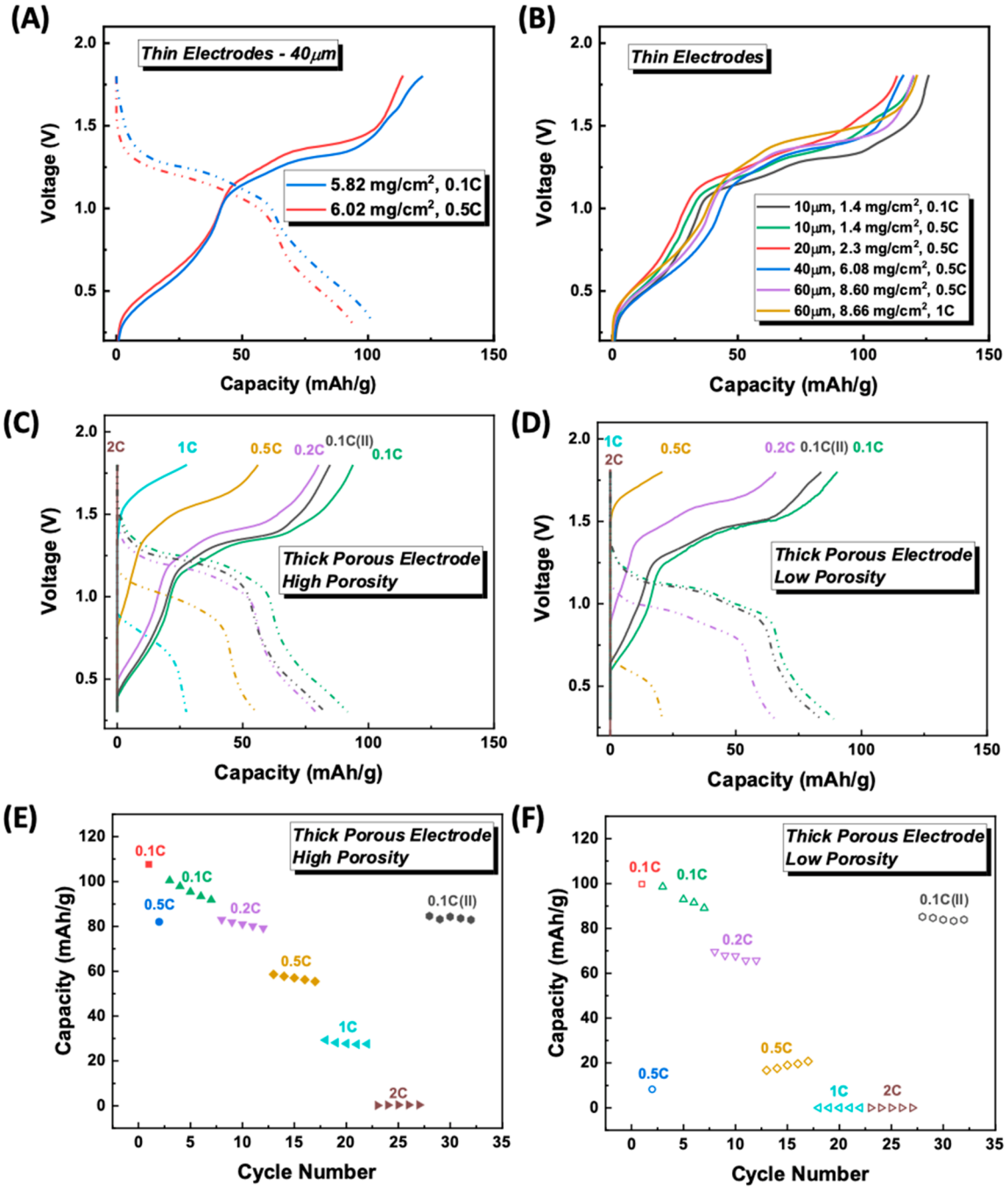

Figure 2. Electrochemical cycling profiles of LiV_3O_8−$LiMn_2O_4$ coupled electrode with various thicknesses in WIS ($Li(TFSI)_{0.7}(BETI)_{0.3}·2H_2O$) cells. (A) Representative charging−discharging curves of thin electrodes (40 μm) cycled under 0.1C and 0.5C rates. (B) Charging behaviors of thin electrodes (10−60 μm) cycled under 0.5C rate, and electrodes with two boundary conditions: 10 μm thickness at 0.1C rate, and 60 μm thickness at 1C rate. (C−F) Rate-dependent performance of thick porous LiV_3O_8−$LiMn_2O_4$ coupled electrodes in WIS ($Li(TFSI)_{0.7}(BETI)_{0.3}·2H_2O$) cells with different porosities [(C, E): high porosity (75%); (D, F): low porosity (60%)].

(pentafluoroethanesulfonyl)imide (LiBETI) in a formula of $Li(TFSI)_{0.7}(BETI)_{0.3}·2H_2O$.[15] The LVO−LMO couple provides a high capacity, moderate voltage range, and good X-ray imaging contrast.[41] Prior studies with dilute organic electrolyte indicated that the ionic diffusion in the porous electrode matrix, instead of the solid-phase diffusion in the active material, is the primary limitation in the spinel $LiMn_2O_4$ cycled under the higher rate;[42−44] samples showed higher degrees of delithiation toward the surface of the electrode, leading to a gradient of delithiation into the depth of the electrode.[44] However, our prior work using spectroscopic imaging to map the chemical gradient in a thin LMO electrode in a LVO−LMO battery with WIS electrolyte did not exhibit such chemical gradients.[41] It is thus of particular interest to investigate the chemical homogeneity of LMO within thick porous electrodes (TPEs) in ultrahighly concentrated aqueous electrolytes. By probing the spatial chemical heterogeneity, the multimodal results indicate that the ionic diffusion in the electrolyte is the primary rate-limiting factor.

https://doi.org/10.1021/acscentsci.1c00878
ACS Cent. Sci. XXXX, XXX, XXX−XXX

RESULTS AND DISCUSSIONS

To characterize the electrochemistry in WIS batteries, Raman tomography, *operando* X-ray powder diffraction (XPD), and three-dimensional (3D) X-ray absorption near-edge structure (XANES) were conducted to address this issue by visualizing chemical heterogeneities. Their experimental setups are illustrated in Figure 1. 3D Raman spectroscopy maps the distribution of active material, conductive additive, and electrolyte in the electrodes to characterize the electrolyte pathway in thick electrodes.[45] *Operando* XPD refinement and Pseudo-Voigt profile fitting provide the information on phase transformation during cycling.[46] 3D XANES spectroscopic imaging, also known as XANES tomography, enables spatially resolved quantification of the chemical states of electrodes.[47−49] The LVO−LMO WIS cells with thick porous electrodes (150−230 μm) of different porosities and conventional casted thin electrodes (10−60 μm) were compared under different cycling rates. For the thick electrode, freestanding electrodes with multiwalled carbon nanotubes (MWCNTs) are utilized to enable high electrical conductivity as well as provide the structure integrity throughout the electrode, hence mitigating the consideration on the electrical conductivity altered by creating thicker electrodes; the discussion can thus focus on the ionic transport, as the electron transport is expected to be sufficiently fast compared to the ionic transport. This work focuses on studying the Li^+ extraction from the LMO cathode and the Li^+ intercalation into the LVO anode. The reaction equations for the cathode and anode are shown below:

$$\text{Cathode: } LiMn_2O_4 \rightarrow Li_{1-x}Mn_2O_4 + xLi^+ + xe^-$$

$$\text{Anode: } xLi^+ + xe^- + LiV_3O_8 \rightarrow Li_{1+x}V_3O_8$$

The x range is $0 \leq x \leq 1$ according to the voltage range of the cycling and the cathode-to-anode mass ratio. Note that LVO during an intercalation reaction can accommodate up to ∼1.5 Li equiv.[50] The electrochemical cycling profiles of LVO−LMO WIS batteries with various thicknesses, porosities, and rate-dependent behaviors are shown in Figure 2. Figure 2A shows the representative first full-cycle curves of the thin electrodes (40 μm) cycled under 0.1C and 0.5C rates, which are consistent with the previous report.[41] Figure 2B shows the initial charging capacity of thin electrodes a range of varying thickness (10−60 μm) cycled under a 0.5C rate, as well as two boundary conditions of electrodes with the smallest thickness cycled at the slowest rate (10 μm at 0.1C) and with the largest thickness cycled at the fastest rate (60 μm at 1C). Figure 2 C,E and D,F show the rate-dependent cycling performance of high-porosity (HP) TPEs and low-porosity (LP) TPEs, respectively. As shown in Figure 2, although the cells with thin electrodes deliver more capacity at 0.1C rate than 0.5C or 1C rates, the charging capacities under 0.5C and 1C rate are close, ∼80% of LMO theoretical capacity (148 mAh g^{-1}).[51] However, the charging capacities of TPEs (>150 μm) are highly rate-dependent in Figure 2C−F. Note that the HP TPEs also exhibit better rate performance than the LP TPEs. The rate-dependent behavior in the thick electrodes implies that there are kinetic limiting factors in the system, which could be solid-state diffusion of Li ions within the electrodes, interfacial reactions of the lithiation/delithiation processes, and liquid-phase diffusion of ions in the WIS electrolyte. Some studies already reported that the solid-phase diffusion of Li ions is not the rate-limiting step of LMO electrodes in the nonaqueous, dilute electrolytes,[42] and the ion transport in the electrolyte plays a key role in thick electrodes.[31] In addition, the rates of solid-state diffusion of Li ions and interfacial reactions do not vary between thin and thick electrodes. As a result, the rate-dependent behavior of TPEs indicates the ionic diffusion in the electrolyte remains as the primary rate-determining step. To support this inference, the bulk phase transformation and local chemical evolution were carried out to map the chemical heterogeneity of $Li_xMn_2O_4$ ($0 \leq x \leq 1$) during delithiation in both thin and thick electrodes. The 3D Raman mapping was applied to TPEs for understanding the pathways of WIS electrolyte in the thick electrodes.

Figure S2A shows the *operando* XPD patterns of a thin (60 μm) electrode cycled under a 0.5C rate during the first charging half-cycle which delivered ∼80% capacity. The peak evolution of $Li_xMn_2O_4$ (111) and (311) in Figure S2B shows a continuous phase change along the charging process. The Pseudo-Voigt fitting $Li_xMn_2O_4$ (111) and (311) peak profiles at the fully charge state shown in Figure S2C can both be deconvoluted into two peaks at the fully charged state, demonstrating that two phases coexist in the end product of thin LMO electrode in WIS cells. The results of phase evolution and Bragg peak separation are consistent with the previous reports conducted in non-aqueous electrolytes.[52−54] According to the phase diagram, the delithiation of LMO changes from a solid-solution phase (α-phase) into a two-phase reaction where one phase is $Li_{0.4-0.6}Mn_2O_4$(β-phase) and the other is λ-Mn_2O_4 (λ-phase).[52−55] As a result, one of the deconvoluted peaks in Figure S2C is attributed to the β-phase, which is located at a lower 2θ angle and has a longer lattice parameter due to less delithiation. The other peak corresponds to λ-phase, which is completely delithiated with a shorter lattice parameter at a higher diffraction angle. The fitting parameters of Figure S2C summarized in Table S2 show that one of the two phases is β-phase with a larger lattice parameter, while the other one is λ-phase with a smaller lattice parameter. The local chemical evolution investigated by XANES tomography provides information that is complementary to bulk diffraction. Through mapping the white line position of each pixel in the sample, the 3D chemical distribution in the post-charged $LiMn_2O_4$ thin electrode (60 μm, fully charged under 0.5C in Figure 2B) is visualized in Figure S3. The white line position as represented by the color scale ranging from 6560 to 6562 eV directly corresponds to the chemical states of LMO electrode: ∼6560 eV corresponds to a pristine state ($Mn^{3.5+}$) and ∼6562 eV corresponds to a fully delithiated state (Mn^{4+}).[56,57] From the 3D visualization (Figure S3A) and histogram (Figure S3B) of chemical states, the thin LMO electrode exhibits some chemical heterogeneities during the delithiation process. The histogram of the chemical distribution in Figure S3B could be decomposed into two peak profiles. Each peak represents an oxidation state of Mn in $Li_xMn_2O_4$ ($0 \leq x \leq 1$), so the presence of two peaks here is consistent with the two phases identified in the XPD fitting results of Figure S2C. Although the incomplete reaction, i.e., the chemical heterogeneity of $Li_xMn_2O_4$, is found in the histogram (Figure S3B), the chemical mapping (Figure S3A) shows a similar spatial distribution of chemical states from the surface near the separator to the bottom near the current collector, which indicates that this chemical heterogeneity occurred consistently across the thickness of the electrode. This is consistent with the fact that the cells with thin electrodes do not show rate-dependent behaviors.

To ensure the wettability of highly concentrated electrolyte in the TPEs, Raman mapping was used to visualize the percolation

https://doi.org/10.1021/acscentsci.1c00878
ACS Cent. Sci. XXXX, XXX, XXX−XXX

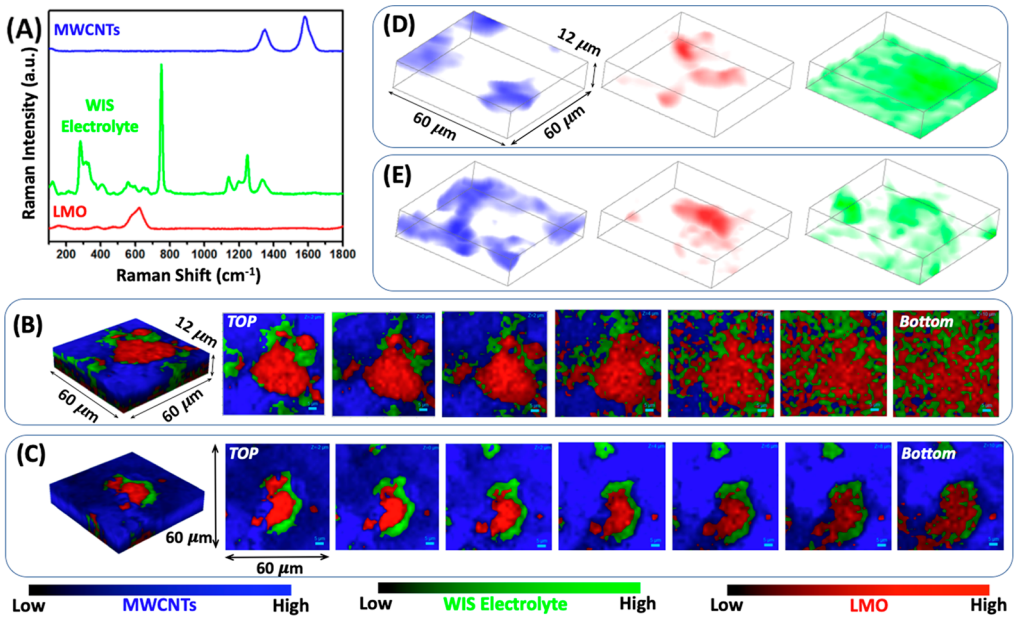

Figure 3. Raman spectra of the LMO, the WIS electrolyte ($Li(TFSI)_{0.7}(BETI)_{0.3}\cdot 2H_2O$), and the MWCNTs. (A) Confocal 3D Raman of merged signals and individual components within the mapped electrode volume: HP TPE (B and D), LP TPE (C and E). Red: LMO, green: WIS electrolyte, and blue: MWCNTs. 2D Raman maps of HP TPE (B) and LP TPE (C) at different electrode depths. Top left: electrode surface, bottom right: 12 μm below electrode surface. Maps (B) and (C) were generated using CLS component mapping, while maps (D) and (E) were obtained using the NMF component mapping procedure. Animated versions of (D) and (E) are available as Supporting Information.

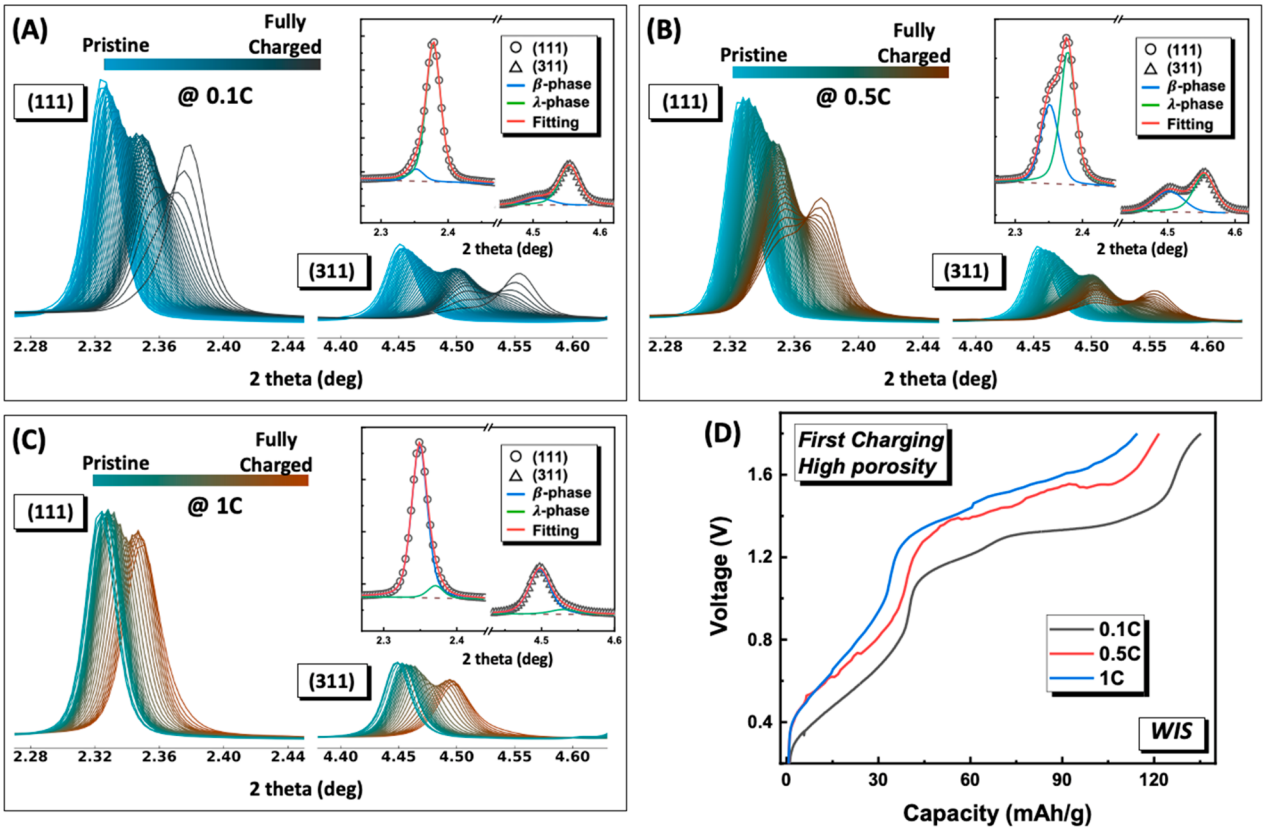

Figure 4. *Operando* XPD patterns of high-porosity thick electrode cycled under 0.1C, 0.5C, and 1C rates, which delivered 91.4%, 82.2%, and 77.4% $LiMn_2O_4$ theoretical capacity, respectively. (A–C) *Operando* evolutions of the $Li_xMn_2O_4$ (111) and (311) diffraction peaks cycled under 0.1C, 0.5C, and 1C rates, respectively. The inset figures in (A–C) show the fitting profiles of (111) and (311) peaks at fully charged state via Pseudo-Voigt method. (D) Electrochemical profiles of *operando* WIS ($Li(TFSI)_{0.7}(BETI)_{0.3}\cdot 2H_2O$) cells presenting in (A–C).

of WIS electrolyte in the electrodes. Raman spectroscopy allows for interrogation of materials with both high and low crystallinity and is sensitive to various metal oxides, carbonaceous materials, and aqueous electrolytes, which render the capability of probing

https://doi.org/10.1021/acscentsci.1c00878
ACS Cent. Sci. XXXX, XXX, XXX−XXX

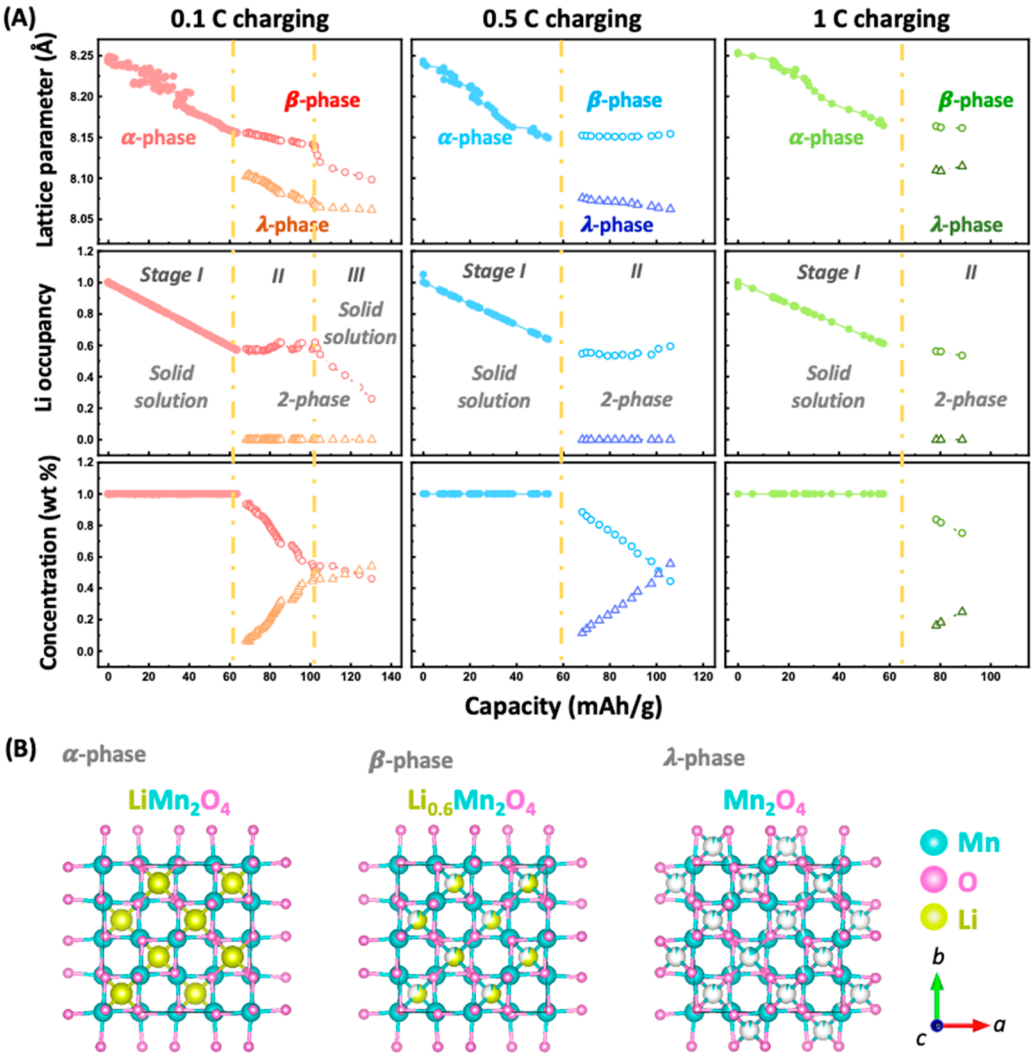

Figure 5. X-ray diffraction refinement analysis for the *operando* study of HP LMO evolution in a WIS electrolyte ($Li(TFSI)_{0.7}(BETI)_{0.3}{\cdot}2H_2O$). (A) Evolution of the lattice parameter and Li atomic occupancy (x in $Li_xMn_2O_4$) of HP electrodes charged under 0.1C, 0.5C, and 1C rates. (B) Crystal structures of the phases from the XPD refinement.

the wetting and distribution of WIS electrolyte within the LMO HP and LP TPEs. 3D confocal Raman mapping of WIS electrolyte containing TPEs has been conducted to offer a true chemical view of mesoscale electrode structures and the internal Li-ion transport pathways. The Raman spectra of LMO, WIS electrolyte, and MWCNTs are displayed in Figure 3A. The classical least-squares (CLS) rendered merged 3D maps are depicted in Figure 3B,C for the HP and LP TPEs, where the red, green, and blue signals represent LMO, WIS electrolyte, and MWCNTs, respectively. The same set of spectra were processed using non-negative matrix factorization (NMF), which has been well-described elsewhere.[58,59] The spectra were normalized to account for the loss of Raman signal intensity with increasing sampling depth and further preprocessed to estimate and subtract the signal baseline. The NMF rendered 3D distribution of individual components are displayed in Figure 3D,E, respectively, for the HP and LP TPEs.

To further investigate the pathways of WIS electrolyte within the TPEs, CLS-rendered 2D Raman maps of the HP and LP TPEs at each electrode depth are summarized in Figure 3B,C. In general, the WIS electrolyte tends to flow through the pores between LMO aggregates and MWCNTs, especially in the low porosity electrodes, as indicated by the green map following the contour of red map in Figure 3C,E. This can be possibly attributed to the gap/pores between MWCNTs and LMO (>5 μm) being much larger than those within MWCNTs or LMO itself (<2 μm), which facilitate the flow of viscous WIS electrolyte. Due to the limited large and accessible pores available in the LP TPE, the percolation of WIS electrolyte (Li-ion) is drastically reduced (Figure 3E), which can potentially lead to impedance in ion transport and poor rate performance of the cell.

The *operando* XPD results of thick porous LiV_3O_8−$LiMn_2O_4$ WIS cell cycled under 0.1C, 0.5C, and 1C rates are shown in Figure S4 (LP, 60% porosity) and Figure S5 (HP, 75% porosity). Since the thick electrodes are a free-standing porous structure, there are no diffraction peaks from the current collectors, e.g., aluminum. To evaluate the LMO phase transformation, the *operando* evolution of $Li_xMn_2O_4$ (111) and (311) peak profiles and analysis results through pseudo-Voigt fitting are shown in Figure S6 (LP, 60% porosity) and Figure 4 (HP, 75%). The LP cells deliver 90.2%, 75%, and 78% $LiMn_2O_4$ theoretical capacity under 0.1C, 0.5C, and 1C, respectively. From the fitting results in Figure S6A−C and Table S2, only the 0.1C rate in LP cells

https://doi.org/10.1021/acscentsci.1c00878
ACS Cent. Sci. XXXX, XXX, XXX−XXX

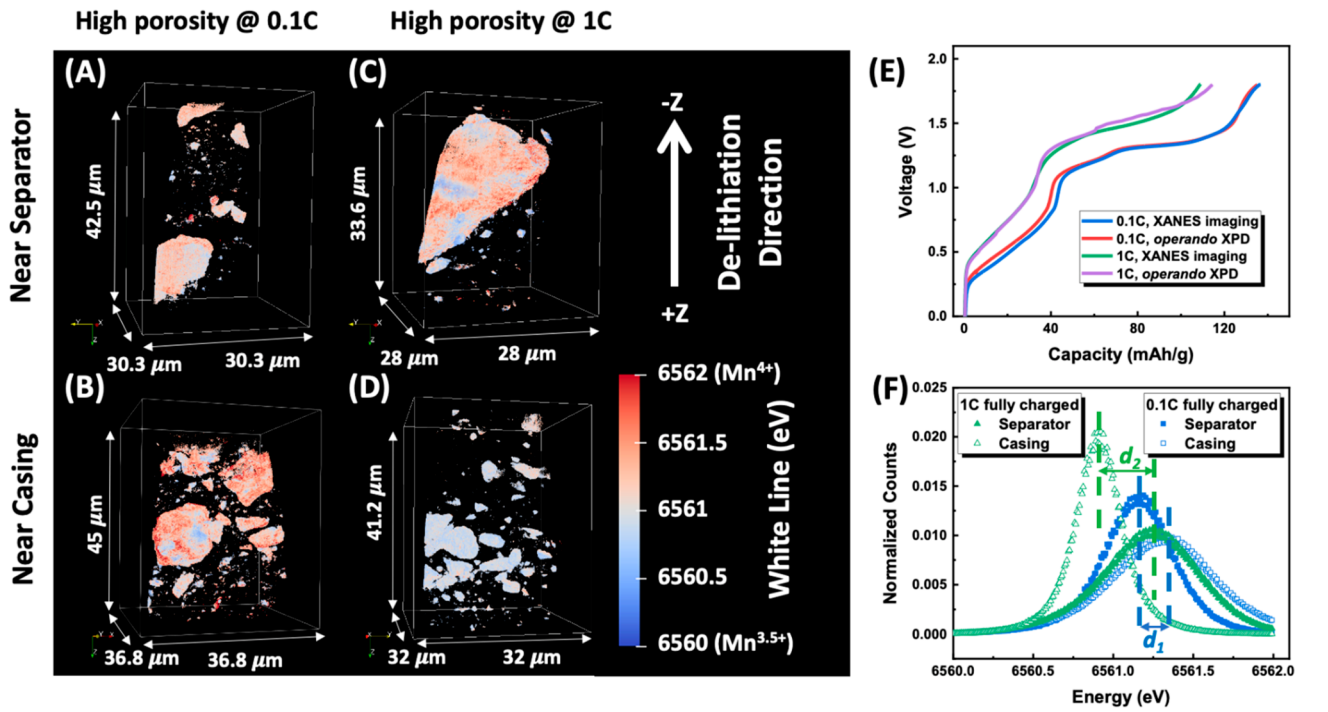

Figure 6. Chemical distribution of high-porosity thick porous $LiMn_2O_4$ electrode cycled under different C rates in WIS ($Li(TFSI)_{0.7}(BETI)_{0.3}{\cdot}2H_2O$) cells (A,B) 0.1C; (C,D) 1C and at different positions [near separator (A,C) vs near casing (B,D)]. (E) Electrochemical profiles of the charging process under different C rates and measurements. (F) Histogram of chemical distribution with different rates and positions. Movies of (A−D) are available in Supporting Information.

leads to the coexistence of two phases in the end product of $LiMn_2O_4$ electrode. In contrast, only β-phase, which is less delithiated, is identified at the fully charged state under 0.5C and 1C rates in the LP LMO electrode. The delivered capacity does not follow a specific trend as a function of the cycling rate. Therefore, it implies that there are other limiting factors in the LP WIS cell under the high C rates (0.5C vs 1C). More morphological analysis not covered in this work, such as the pore size distribution or the spatial distribution of the pores, may need to be carried out to fully understand the 3D structure of the LP TPEs and its impact on the performance.

In contrast, the *operando* $Li_xMn_2O_4$ peaks and the two-phase reaction analyzed through Pseudo-Voigt fitting shown in Figure 4 for the HP TPEs are consistent with the trend shown in the electrochemical results. To further validate the evolutionary trend of the LMO phase in HP electrodes, *operando* Rietveld refinement was conducted. Figure S7 shows the individual refined diffraction profile of the pristine state and fully charged state under 0.1C, 0.5C, and 1C rates. Each component of the initial and final states is well-resolved and labeled accordingly in Figure S7. A discrepancy between the refinement and the data can be found at ∼3 deg in Figure S7 (0.1C fully charged). The peak corresponds to the LVO ($\bar{1}03$), and the deviation is due to a strong preferred orientation of the LVO. The diffraction patterns of LMO and LVO are overlapped because the *operando* measurements were conducted in a transmission geometry. The relative concentration of the LMO phases is thus independent of the LVO phases. The refined parameters including the lattice parameter, Li atomic occupancy (x in $Li_xMn_2O_4$), and relative concentration (in wt % normalized to the LMO phases) are summarized in Figure 5 and Figure S8. The capacities deriving from the amount of phase transformation in Figure S8 and Table S3 are consistent with the electrochemical performance under 0.1C and 0.5C rates. The deviation of capacities under the 1C rate implies an inhomogeneous distribution of the local oxidation state. Nevertheless, the reaction with a faster rate (1C) still reflects a greater chemical heterogeneity than the slower rates (0.1C or 0.5C). The *operando* evolution of the lattice parameter and Li atomic occupancy in Figure 5 also agree with the previous reports.[53,55] The refinement also shows that, when the delivered capacity is larger than ∼60 mAh g^{-1}, the delithiation of LMO changes from a solid-solution reaction (α-phase) into a two-phase reaction where one phase is $Li_{0.5-0.6}Mn_2O_4$ (β-phase) and the other is λ-Mn_2O_4 (λ-phase). These observations strengthen the reliability of the *operando* refinement results. Therefore, in Figure 4A−C, Figure S8, and Table S2, the dominant phase in the 0.1C fully charged HP LMO is λ-phase. While the C rate increases, the ratio of the λ-phase decreases, and the ratio of β-phase increases. In the 1C fully charged case, the β-phase becomes the dominated phase. Overall, the ratios between β- and λ-phase are consistent with the delivered capacities in HP electrodes and also reflect the average structural/chemical inhomogeneity under different C rates.

More specifically, Figure 5 shows the rate effects in the LMO phase. At the 0.1C rate, the delithiation manifests first in the decrease of lithium occupancy in the solid-solution phase (α-phase) (*Stage I*, solid-solution region) and at about 60 mAh g^{-1}, the Li occupancy holds at ∼0.6 (β-phase), while the Li-poor phase (λ-phase) starts to appear, further decreasing the overall Li contents in the LMO structure (*Stage II*). At about 100 mAh g^{-1}, the Li occupancy in the solid-solution phase (β-phase) starts to decrease again, contributing to the capacity of the cell (*Stage III*). At the 0.5C rate, the delithiation stops at the end of *Stage II*, and at the 1C rate, it stops at approximately halfway of *Stage II*. Therefore, the phase evolution detected by the *operando* XPD

https://doi.org/10.1021/acscentsci.1c00878
ACS Cent. Sci. XXXX, XXX, XXX−XXX

with refinement analysis supports that the rate limit is on the LMO side. Combined with the XANES tomography (Figure 6, discussed in the next section), which shows the spatial inhomogeneity in the Mn valence state, the results further confirmed that the kinetic limitation is from the electrolyte in the porous space in LMO.

Since the HP TPEs hold a good percolation of WIS electrolyte as shown in Figure 3D, the rate-limiting factor of delithiation in HP LMO electrodes could be determined by observing the spatial distribution of the Li ion concentration in electrodes. Thus, the local chemical distributions of TPEs were analyzed by *ex situ* 3D XANES tomography via selecting two regions of interest: one near the separator and one near the casing. 3D XANES enables spatially quantifying the distribution of chemical states within the electrode at the two most distinct locations relative to the ionic diffusion distance from the anode. To alleviate the concern of chemical state redistribution, the *ex situ* samples were dried under vacuum once the cells reached the cutoff voltage. The redistribution within individual particles may still exist but does not impact the chemical mapping across the entire electrode. As shown in Figure 6, the chemical state distributions of HP LMO electrodes fully charged to 1.8 V at 0.1C and 1C rates are mapped in 3D by XANES tomography at both regions: near the separator as shown in Figure 6A,C and near the casing as shown in Figure 6B,D. Figure 6E shows the capacity profiles of all the tested cells from the first-charging half cycle, which deliver 91.4% and 77.4% of LMO theoretical capacity for 0.1C and 1C rates, respectively. The histogram in Figure 6F presents the statistical distribution of the chemical states in Figure 6A−D. The chemical mapping in Figure 6A−D shows that the HP LMO electrode cycled under a 0.1C rate has an overall more complete reaction than that cycled under a 1C rate. The two closer peaks in the blue curves in Figure 6F represent the major λ-phase with some minor β-phase which distributes uniformly in the electrode under the 0.1C rate. On the other hand, the less complete reaction at the 1C rate is expected according to the electrochemical data and is consistent with the XPD results shown in Figure 4 and Figure 5, where the dominant phase in the fully charged product at the 1C rate remains the β-phase. At the 1C rate, the region near the casing has a lower extent of delithiation and a higher degree of chemical homogeneity than the near-separator region. In Figure 6F, the peak with higher white line energy in the green solid curves represents the λ-phase concentrates in the region near separator under a 1C rate. The one with a lower white line energy in the green curves represents the β-phase dominating in the region near casing.

The different extents of heterogeneity ($d_2 = 0.35 > d_1 = 0.15$ eV) shown in Figure 6 F for the different regions under the same rate also shows that there is more chemical heterogeneity under 1C than under 0.1C. Figure 6F also shows that the regions near separator (shorter Li-ion diffusion distance) at both 0.1C and 1C rates have a similar level of delithiation (within XANES energy fitting resolution). In contrast, the region near casing at 0.1C rate has a closer level of delithiation to the regions near the separator than at 1C, but the region near casing at the 1C rate shows the least complete delithiation in Figure 6. The inhomogeneous chemical distribution from the near-separator region to the near-casing region at the 1C rate indicates that the ion transport limitation leads to a gradient of Li ion along the voltage bias direction in the thick porous $LiMn_2O_4$ electrode, causing a less complete delithiation reaction near the casing. By combining the rate-dependent behaviors, Raman mapping, bulk diffraction, and local chemical mapping, ionic diffusion in the electrolyte is suggested as the primary rate-limiting factor in the thick porous LiV_3O_8−$LiMn_2O_4$ electrode couple reacted in WIS electrolyte. If the reaction is limited by other factors rather than by the long-range ionic diffusion in the electrolyte, such as solid-state diffusion in LMO or LVO, interfacial diffusion through SEI, or other interfacial reactions, the concentration of Li ions in the electrolyte should be homogeneous and thus lead to no chemical heterogeneity in LMO. Note that according to our previous study,[41] the Mn dissolution can be significantly suppressed when cycling in WIS electrolyte. Therefore, the inhomogeneity of the Mn valence state is primarily attributed to the reaction heterogeneity. The spatial chemical heterogeneity along the bias direction in LMO is a direct indication that the kinetics is limited by the long-range ionic diffusion in the electrolyte.

Figure 7 shows a schematic summary of the rate-limiting behavior for the thicker porous electrode of LMO in the WIS

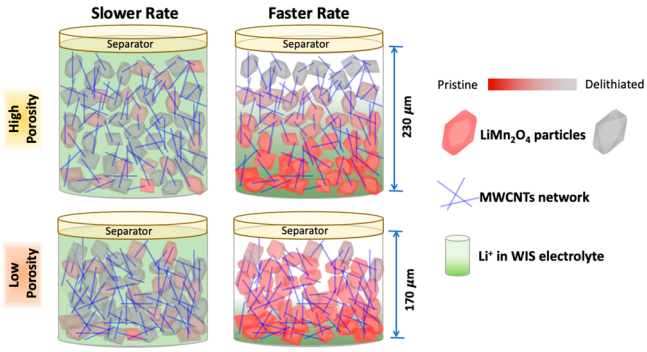

Figure 7. Schematics of rate-limiting behavior for the faster cycling rate in the thick porous electrode of LMO, in WIS electrolyte. While there is a significant amount of Li ions, the slower Li ion diffusion rate in the WIS electrolyte leads to a rate-limiting behavior and chemical heterogeneity, which is also more prominent in the lower porosity electrode. Future work in theoretically modeling the transport phenomena in the WIS electrolyte, tuning the electrode design to mitigate the slower Li-ion diffusion in WIS electrolyte, as well as designing the WIS electrolyte with enhanced ionic diffusivity will hold crucial keys to enhance the rate performance of aqueous Li-ion batteries with high voltage and high loading.

electrolyte, in which Li ion diffusivity is lower than that of conventional dilute electrolytes, although the Li ion concentration is significantly higher. As the reaction rate increases, less time is allowed for the Li-ion to diffuse, leading to a chemical heterogeneity and reaction-state gradient in LMO along the thickness direction. This effect is further enhanced when the porosity is reduced, which leads to a decreased effective diffusivity, D_{eff}, as discussed in the Introduction, causing further chemical heterogeneity and incomplete reactions. Such behavior can be mitigated by designing electrodes with lower tortuosity and enhancing the Li-ion diffusivity in the electrolyte; further modeling and theoretical work could also be essential to quantitatively understand the complex behavior concerning the electrochemical reaction kinetics, electrolyte−electrode interfaces, and transport phenomena in porous electrodes. Future work may also consider testing the systems with different separators, such as glass fiber separators, to study the effect of varying wettability in the transport phenomena.

https://doi.org/10.1021/acscentsci.1c00878
ACS Cent. Sci. XXXX, XXX, XXX−XXX

CONCLUSION

Aqueous batteries with high mass-loading electrodes (thick porous electrodes) were successfully fabricated and demonstrated promising performance in a WIS electrolyte. The electrochemistry of a WIS battery based on LiV_3O_8 as the anode and $LiMn_2O_4$ as the cathode was investigated to understand the transport phenomena with various thicknesses—in thin electrodes (10−60 μm) and thick porous electrodes (150−230 μm)—cycled under 0.1C to 1C rates. In the first charging cycles, the thick electrodes show a rate dependency, while thin electrodes do not exhibit rate dependency. This result implies the ionic diffusion in the electrolyte as the primary rate-limiting factor for thick porous electrodes in LiV_3O_8−$LiMn_2O_4$ WIS systems.

The observation of the electrochemical behaviors was further verified by characterizing the percolation, phase transformation, and chemical heterogeneity in the $LiMn_2O_4$ electrodes through Raman mapping, *operando* XPD, and *ex situ* XANES tomography. The Raman mapping shows a better percolation of the WIS electrolyte in the high-porosity thick electrode than the low-porosity one. The excellent wettability of the WIS electrolyte within the high-porosity structure facilitates the ion transportation. The *operando* XPD reveals the bulk phase transformation of $LiMn_2O_4$ through pseudo-Voigt profile fitting. For high-porosity thick electrodes, the formation of the λ-phase (complete delithiation) is observed under all tested rates, whereas the λ-phase is only found under a 0.1C rate in a low-porosity thick electrode. The existence of the λ-phase indicates that the rate capability is promoted because of the increased porosity, thus enhancing the ionic diffusion. The varying ratio between β- vs λ-phase under various C rates is also consistent with the kinetics limitation in the high-porosity thick electrode.

The local distribution of the chemical state in post-cycled $LiMn_2O_4$ electrodes was visualized and quantified in 3D by XANES tomography. In chemical mapping and histogram of 3D XANES, the thin $LiMn_2O_4$ electrode (60 μm) shows a homogeneous chemical distribution. However, the chemical state distribution in the high-porosity thick $LiMn_2O_4$ electrode (~230 μm) under the 1C rate has spatial heterogeneities from the surface near separator to the region near casing. By comparing the chemical distribution spatially under 0.1C vs 1C, the results consistently show that the ionic diffusion in the electrolyte may be the rate-limiting factor in this system. By determining the rate-limiting factor via probing the electrolyte pathway and chemical heterogeneities, our study enhances the understanding of the transport phenomena of the WIS electrolyte in $LiMn_2O_4$ electrodes. A clear insight of the kinetic limitations in highly concentrated electrolytes and thick porous structures sheds light on high energy density applications. This work also provides a framework for studying the kinetics in an electrochemically driven system toward the strategies to design advanced batteries. Future work in theoretically modeling the transport phenomena in the WIS electrolyte, tuning the electrode design to mitigate the slower Li-ion diffusion in the WIS electrolyte, as well as designing the WIS electrolyte with enhanced ionic diffusivity will hold crucial keys to enhance the rate performance of aqueous Li-ion batteries with high voltage and high loading.

ASSOCIATED CONTENT

Supporting Information

The Supporting Information is available free of charge at https://pubs.acs.org/doi/10.1021/acscentsci.1c00878.

Experimental section; additional tables summarizing the physiochemical properties of the electrolytes, the Pseudo-Voigt fitting parameters, and the comparison of delivered capacities; additional figures including *operando* XPD, Rietveld refinement, Pseudo-Voigt peak fitting, SEM image, XANES tomography, and Raman tomography (PDF)

Video S1: Raman Mapping of MWCNTs in the HP TPE (MP4)

Video S2: Raman Mapping of LMO in the HP TPE (MP4)

Video S3: Raman Mapping of WIS electrolyte in the HP TPE (MP4)

Video S4: Raman Mapping of MWCNTs, LMO, and WIS electrolyte in the HP TPE (MP4)

Video S5: Raman Mapping of MWCNTs in the LP TPE (MP4)

Video S6: Raman Mapping of LMO in the LP TPE (MP4)

Video S7: Raman Mapping of WIS electrolyte in the LP TPE (MP4)

Video S8: Raman Mapping of MWCNTs, LMO, and WIS electrolyte in the LP TPE (MP4)

Video S9: XANES mapping of HP LMO near separator cycled under 0.1 C rate (MP4)

Video S10: XANES mapping of HP LMO near casing cycled under 0.1 C rate (MP4)

Video S11: XANES mapping of HP LMO near separator cycled under 0.1 C rate (MP4)

Video S12. XANES mapping of HP LMO near casing cycled under 0.1 C rate (MP4)

AUTHOR INFORMATION

Corresponding Authors

Mingyuan Ge − *National Synchrotron Light Source II, Brookhaven National Laboratory, Upton, New York 11973, United States*; Email: mingyuan@bnl.gov

Yu-chen Karen Chen-Wiegart − *Department of Materials Science and Chemical Engineering, Stony Brook University, Stony Brook, New York 11794, United States; National Synchrotron Light Source II, Brookhaven National Laboratory, Upton, New York 11973, United States;* orcid.org/0000-0003-4445-2159; Email: Karen.Chen-Wiegart@stonybrook.edu

Authors

Cheng-Hung Lin − *Department of Materials Science and Chemical Engineering, Stony Brook University, Stony Brook, New York 11794, United States;* orcid.org/0000-0001-9254-9751

Lei Wang − *Energy and Photon Sciences Directorate, Brookhaven National Laboratory, Upton, New York 11973, United States;* orcid.org/0000-0002-6348-8344

Steven T. King − *Department of Chemistry, Stony Brook University, Stony Brook, New York 11794, United States*

Jianming Bai − *National Synchrotron Light Source II, Brookhaven National Laboratory, Upton, New York 11973, United States;* orcid.org/0000-0002-0575-2987

https://doi.org/10.1021/acscentsci.1c00878
ACS Cent. Sci. XXXX, XXX, XXX−XXX

Lisa M. Housel − *Department of Chemistry, Stony Brook University, Stony Brook, New York 11794, United States;* orcid.org/0000-0001-8429-5480
Alison H. McCarthy − *Department of Materials Science and Chemical Engineering, Stony Brook University, Stony Brook, New York 11794, United States*
Mallory N. Vila − *Department of Chemistry, Stony Brook University, Stony Brook, New York 11794, United States*
Hengwei Zhu − *Department of Chemistry, Stony Brook University, Stony Brook, New York 11794, United States*
Chonghang Zhao − *Department of Materials Science and Chemical Engineering, Stony Brook University, Stony Brook, New York 11794, United States;* orcid.org/0000-0002-3538-6199
Lijie Zou − *Department of Materials Science and Chemical Engineering, Stony Brook University, Stony Brook, New York 11794, United States; State Key Lab of Advanced Technology for Materials Synthesis and Processing, Wuhan University of Technology, Wuhan 430070, China*
Sanjit Ghose − *National Synchrotron Light Source II, Brookhaven National Laboratory, Upton, New York 11973, United States*
Xianghui Xiao − *National Synchrotron Light Source II, Brookhaven National Laboratory, Upton, New York 11973, United States*
Wah-Keat Lee − *National Synchrotron Light Source II, Brookhaven National Laboratory, Upton, New York 11973, United States*
Kenneth J. Takeuchi − *Department of Materials Science and Chemical Engineering, Stony Brook University, Stony Brook, New York 11794, United States; Department of Chemistry, Stony Brook University, Stony Brook, New York 11794, United States;* orcid.org/0000-0001-8129-444X
Amy C. Marschilok − *Department of Materials Science and Chemical Engineering, Stony Brook University, Stony Brook, New York 11794, United States; Energy and Photon Sciences Directorate, Brookhaven National Laboratory, Upton, New York 11973, United States; Department of Chemistry, Stony Brook University, Stony Brook, New York 11794, United States;* orcid.org/0000-0001-9174-0474
Esther S. Takeuchi − *Department of Materials Science and Chemical Engineering, Stony Brook University, Stony Brook, New York 11794, United States; Energy and Photon Sciences Directorate, Brookhaven National Laboratory, Upton, New York 11973, United States; Department of Chemistry, Stony Brook University, Stony Brook, New York 11794, United States;* orcid.org/0000-0001-8518-1047

Complete contact information is available at: https://pubs.acs.org/10.1021/acscentsci.1c00878

Author Contributions

C-H Lin and Y-cK Chen-Wiegart developed the research concept with inputs from ES Takeuchi and AC Marschilok. C-H Lin, M Ge, and Y-cK Chen-Wiegart designed the synchrotron imaging experiments. C-H Lin, J Bai, S Ghose, and Y-cK Chen-Wiegart designed the synchrotron diffraction experiments. C-H Lin and H Zhu prepared the WiS electrolyte, casted LMO electrodes, and assembled the electrochemical cells, and performed the cycling tests. C-H Lin performed the material analyses by SEM. L Housel, A McCarthy, and M Vila synthesized LiV_3O_8 powders and casted LiV_3O_8 electrodes under the supervision of KJ Takeuchi, ES Takeuchi, and AC Marschilok. L Wang prepared the thick porous electrodes and performed the Raman analysis in collaboration with ST King with input from KJ Takeuchi, ES Takeuchi, and AC Marschilok. C Zhao and L Zou conducted the FIB lift-out sample preparation for imaging. C-H Lin, H Zhu, C Zhao, and Y-cK Chen-Wiegart conducted the synchrotron diffraction experiments with the XPD beamline staff support by J Bai and S Ghose. C-H Lin, C Zhao, and Y-cK Chen-Wiegart conducted the synchrotron imaging experiments with the FXI beamline staff support by M Ge, X Xiao, and W-K Lee. C-H Lin and H Zhu performed the diffraction data analysis under the guidance of J Bai and Y-cK Chen-Wiegart. C-H Lin performed the 3D XANES imaging data analysis under the guidance of Y-cK Chen-Wiegart, M Ge. C-H Lin wrote the manuscript under the supervision of Y-cK Chen-Wiegart, with the inputs from all coauthors.

Notes

The authors declare no competing financial interest.

■ ACKNOWLEDGMENTS

The work was supported as part of the Center for Mesoscale Transport Properties (m2M/t), an Energy Frontier Research Center funded by the U.S. Department of Energy, Office of Science, Basic Energy Sciences, under Award # DE-SC0012673. This research used resources, Full Field X-ray Imaging (FXI) beamline (18-ID), and X-ray Powder Diffraction (XPD) beamline (28-ID-2) of the National Synchrotron Light Source II, a U.S. Department of Energy (DOE) Office of Science User Facility operated for the DOE Office of Science by Brookhaven National Laboratory under Contract No. DE-SC0012704. This research used resources of the Center for Functional Nanomaterials (CFN), which is a U.S. DOE Office of Science Facility, at Brookhaven National Laboratory under Contract No. DE-SC0012704. We acknowledge the support on sample preparation, data collection, and preliminary analysis during the FXI beamtime provided by the Chen-Wiegart group members, Xiaoyang Liu, Arthur Ronne, Dean Yen, Lin Chieh Yu, Karol Dyro, and Qingkun Meng. We thank the support provided by the XPD beamline staff, Hui Zhong, for the *operando* experiment set up and data collection. We thank the support provided by the CFN staff, Fernando Camino and Gwen Wright, for the access and training on FIB-SEM and SEM/EDS. A.H. McCarthy acknowledges the Graduate Assistance in Areas of National Need Fellowship (GAANN). E. Takeuchi acknowledges the generous support of the William and Jane Knapp for the Knapp Chair in Energy and the Environment.

■ REFERENCES

(1) Yoo, H. D.; Markevich, E.; Salitra, G.; Sharon, D.; Aurbach, D. On the challenge of developing advanced technologies for electrochemical energy storage and conversion. *Mater. Today* **2014**, *17* (3), 110−121.
(2) Larcher, D.; Tarascon, J. M. Towards greener and more sustainable batteries for electrical energy storage. *Nat. Chem.* **2015**, *7* (1), 19−29.
(3) Tarascon, J. M.; Armand, M. Issues and challenges facing rechargeable lithium batteries. *Nature* **2001**, *414* (6861), 359−367.
(4) Etacheri, V.; Marom, R.; Elazari, R.; Salitra, G.; Aurbach, D. Challenges in the development of advanced Li-ion batteries: a review. *Energy Environ. Sci.* **2011**, *4* (9), 3243−3262.
(5) Liu, J. L.; Xu, C. H.; Chen, Z.; Ni, S. B.; Shen, Z. X. Progress in aqueous rechargeable batteries. *Green Energy Environ.* **2018**, *3* (1), 20−41.
(6) Li, W.; Dahn, J. R.; Wainwright, D. S. Rechargeable Lithium Batteries with Aqueous-Electrolytes. *Science* **1994**, *264* (5162), 1115−1118.

(7) Kim, H.; Hong, J.; Park, K. Y.; Kim, S. W.; Kang, K. Aqueous Rechargeable Li and Na Ion Batteries. *Chem. Rev.* **2014**, *114* (23), 11788−11827.
(8) Kohler, J.; Makihara, H.; Uegaito, H.; Inoue, H.; Toki, M. LiV3O8: characterization as anode material for an aqueous rechargeable Li-ion battery system. *Electrochim. Acta* **2000**, *46* (1), 59−65.
(9) Wang, G. J.; Fu, L. J.; Zhao, N. H.; Yang, L. C.; Wu, Y. P.; Wu, H. Q. An aqueous rechargeable lithium battery with good cycling performance. *Angew. Chem., Int. Ed.* **2007**, *46* (1−2), 295−297.
(10) Wang, G. J.; Zhang, H. P.; Fu, L. J.; Wang, B.; Wu, Y. P. Aqueous rechargeable lithium battery (ARLB) based on LiV3O8 and LiMn2O4 with good cycling performance. *Electrochem. Commun.* **2007**, *9* (8), 1873−1876.
(11) Luo, J. Y.; Xia, Y. Y. Aqueous lithium-ion battery LiTi2(PO4)(3)/LiMn2O4 with high power and energy densities as well as superior cycling stability. *Adv. Funct. Mater.* **2007**, *17* (18), 3877−3884.
(12) Luo, J. Y.; Cui, W. J.; He, P.; Xia, Y. Y. Raising the cycling stability of aqueous lithium-ion batteries by eliminating oxygen in the electrolyte. *Nat. Chem.* **2010**, *2* (9), 760−765.
(13) Suo, L. M.; Borodin, O.; Gao, T.; Olguin, M.; Ho, J.; Fan, X. L.; Luo, C.; Wang, C. S.; Xu, K. Water-in-salt" electrolyte enables high-voltage aqueous lithium-ion chemistries. *Science* **2015**, *350* (6263), 938−943.
(14) Suo, L. M.; Borodin, O.; Sun, W.; Fan, X. L.; Yang, C. Y.; Wang, F.; Gao, T.; Ma, Z. H.; Schroeder, M.; von Cresce, A.; Russell, S. M.; Armand, M.; Angell, A.; Xu, K.; Wang, C. S. Advanced High-Voltage Aqueous Lithium-Ion Battery Enabled by "Water-in-Bisalt" Electrolyte. *Angew. Chem., Int. Ed.* **2016**, *55* (25), 7136−7141.
(15) Yamada, Y.; Usui, K.; Sodeyama, K.; Ko, S.; Tateyama, Y.; Yamada, A. Hydrate-melt electrolytes for high-energy-density aqueous batteries. *Nat. Energy* **2016**, *1*, 9.
(16) Yang, C. Y.; Chen, J.; Qing, T. T.; Fan, X. L.; Sun, W.; von Cresce, A.; Ding, M. S.; Borodin, O.; Vatamanu, J.; Schroeder, M. A.; Eidson, N.; Wang, C. S.; Xu, K. 4.0 V Aqueous Li-Ion Batteries. *Joule* **2017**, *1* (1), 122−132.
(17) Lukatskaya, M. R.; Feldblyum, J. I.; Mackanic, D. G.; Lissel, F.; Michels, D. L.; Cui, Y.; Bao, Z. A. Concentrated mixed cation acetate "water-in-salt" solutions as green and low-cost high voltage electrolytes for aqueous batteries. *Energy Environ. Sci.* **2018**, *11* (10), 2876−2883.
(18) Dahbi, M.; Ghamouss, F.; Tran-Van, F.; Lemordant, D.; Anouti, M. Comparative study of EC/DMC LiTFSI and LiPF6 electrolytes for electrochemical storage. *J. Power Sources* **2011**, *196* (22), 9743−9750.
(19) Borodin, O.; Suo, L. M.; Gobet, M.; Ren, X. M.; Wang, F.; Faraone, A.; Peng, J.; Olguin, M.; Schroeder, M.; Ding, M. S.; Gobrogge, E.; Cresce, A. V.; Munoz, S.; Dura, J. A.; Greenbaum, S.; Wang, C. S.; Xu, K. Liquid Structure with Nano-Heterogeneity Promotes Cationic Transport in Concentrated Electrolytes. *ACS Nano* **2017**, *11* (10), 10462−10471.
(20) Oldiges, K.; Diddens, D.; Ebrahiminia, M.; Hooper, J. B.; Cekic-Laskovic, I.; Heuer, A.; Bedrov, D.; Winter, M.; Brunklaus, G. Understanding transport mechanisms in ionic liquid/carbonate solvent electrolyte blends. *Phys. Chem. Chem. Phys.* **2018**, *20* (24), 16579−16591.
(21) Horwitz, G.; Rodriguez, C. R.; Steinberg, P. Y.; Burton, G.; Corti, H. R. Mobility-viscosity decoupling and cation transport in water-in-salt lithium electrolytes. *Electrochim. Acta* **2020**, *359*, 11.
(22) Li, Z.; Bouchal, R.; Mendez-Morales, T.; Rollet, A. L.; Rizzi, C.; Le Vot, S.; Favier, F.; Rotenberg, B.; Borodin, O.; Fontaine, O.; Salanne, M. Transport Properties of Li-TFSI Water-in-Salt Electrolytes. *J. Phys. Chem. B* **2019**, *123* (49), 10514−10521.
(23) Jeon, J.; Lee, H.; Choi, J. H.; Cho, M. Modeling and Simulation of Concentrated Aqueous Solutions of LiTFSI for Battery Applications. *J. Phys. Chem. C* **2020**, *124* (22), 11790−11799.
(24) Zhang, X.; Ju, Z. Y.; Zhu, Y.; Takeuchi, K. J.; Takeuchi, E. S.; Marschilok, A. C.; Yu, G. H. Multiscale Understanding and Architecture Design of High Energy/Power Lithium-Ion Battery Electrodes. *Adv. Energy Mater.* **2021**, *11* (2), 2000808.
(25) Cheng, H. M.; Li, F. Energy Storage Charge delivery goes the distance. *Science* **2017**, *356* (6338), 582−583.
(26) Zhu, C. B.; Usiskin, R. E.; Yu, Y.; Maier, J. The nanoscale circuitry of battery electrodes. *Science* **2017**, *358* (6369), 8.
(27) Kuang, Y. D.; Chen, C. J.; Kirsch, D.; Hu, L. B. Thick Electrode Batteries: Principles, Opportunities, and Challenges. *Adv. Energy Mater.* **2019**, *9* (33), 19.
(28) Du, Z. J.; Wood, D.; Daniel, C.; Kalnaus, S.; Li, J. L. Understanding limiting factors in thick electrode performance as applied to high energy density Li-ion batteries. *J. Appl. Electrochem.* **2017**, *47* (3), 405−415.
(29) Sun, H. T.; Mei, L.; Liang, J. F.; Zhao, Z. P.; Lee, C.; Fei, H. L.; Ding, M. N.; Lau, J.; Li, M. F.; Wang, C.; Xu, X.; Hao, G. L.; Papandrea, B.; Shakir, I.; Dunn, B.; Huang, Y.; Duan, X. F. Three-dimensional holey-graphene/niobia composite architectures for ultrahigh-rate energy storage. *Science* **2017**, *356* (6338), 599−604.
(30) Hu, J. T.; Wu, B. B.; Cao, X.; Bi, Y. J.; Chae, S. J.; Niu, C. J.; Xiao, B. W.; Tao, J. H.; Zhang, J. G.; Xiao, J. Evolution of the rate-limiting step: From thin film to thick Ni-rich cathodes. *J. Power Sources* **2020**, *454*, 7.
(31) Ju, Z. Y.; Zhu, Y.; Zhang, X.; Lutz, D. M.; Fang, Z. W.; Takeuchi, K. J.; Takeuchi, E. S.; Marschilok, A.; Yu, G. H. Understanding Thickness-Dependent Transport Kinetics in Nanosheet-Based Battery Electrodes. *Chem. Mater.* **2020**, *32* (4), 1684−1692.
(32) Epstein, N. on Tortuosity and the Tortuosity Factor in Flow and Diffusion through Porous-Media. *Chem. Eng. Sci.* **1989**, *44* (3), 777−779.
(33) Chen-Wiegart, Y. C. K.; DeMike, R.; Erdonmez, C.; Thornton, K.; Barnett, S. A.; Wang, J. Tortuosity characterization of 3D microstructure at nano-scale for energy storage and conversion materials. *J. Power Sources* **2014**, *249*, 349−356.
(34) Zacharias, N. A.; Nevers, D. R.; Skelton, C.; Knackstedt, K.; Stephenson, D. E.; Wheeler, D. R. Direct Measurements of Effective Ionic Transport in Porous Li-Ion Electrodes. *J. Electrochem. Soc.* **2013**, *160* (2), A306−A311.
(35) Thorat, I. V.; Stephenson, D. E.; Zacharias, N. A.; Zaghib, K.; Harb, J. N.; Wheeler, D. R. Quantifying tortuosity in porous Li-ion battery materials. *J. Power Sources* **2009**, *188* (2), 592−600.
(36) Xu, K. Nonaqueous liquid electrolytes for lithium-based rechargeable batteries. *Chem. Rev.* **2004**, *104* (10), 4303−4417.
(37) Suo, L. M.; Oh, D.; Lin, Y. X.; Zhuo, Z. Q.; Borodin, O.; Gao, T.; Wang, F.; Kushima, A.; Wang, Z. Q.; Kim, H. C.; Qi, Y.; Yang, W. L.; Pan, F.; Li, J. J.; Xu, K.; Wang, C. S. How Solid-Electrolyte Interphase Forms in Aqueous Electrolytes. *J. Am. Chem. Soc.* **2017**, *139* (51), 18670−18680.
(38) Dubouis, N.; Lemaire, P.; Mirvaux, B.; Salager, E.; Deschamps, M.; Grimaud, A. The role of the hydrogen evolution reaction in the solid-electrolyte interphase formation mechanism for "Water-in-Salt" electrolytes. *Energy Environ. Sci.* **2018**, *11* (12), 3491−3499.
(39) Bouchal, R.; Li, Z. J.; Bongu, C.; Le Vot, S.; Berthelot, R.; Rotenberg, B.; Favier, F.; Freunberger, S. A.; Salanne, M.; Fontaine, O. Competitive Salt Precipitation/Dissolution During Free-Water Reduction in Water-in-Salt Electrolyte. *Angew. Chem., Int. Ed.* **2020**, *59* (37), 15913−15917.
(40) Droguet, L.; Grimaud, A.; Fontaine, O.; Tarascon, J. M. Water-in-Salt Electrolyte (WiSE) for Aqueous Batteries: A Long Way to Practicality. *Adv. Energy Mater.* **2020**, *10* (43), 14.
(41) Lin, C.-H.; Sun, K.; Ge, M.; Housel, L. M.; McCarthy, A. H.; Vila, M. N.; Zhao, C.; Xiao, X.; Lee, W.-K.; Takeuchi, K. J.; Takeuchi, E. S.; Marschilok, A. C.; Chen-Wiegart, Y.-c. K. Systems-level investigation of aqueous batteries for understanding the benefit of water-in-salt electrolyte by synchrotron nanoimaging. *Science Advances* **2020**, *6* (10), No. eaay7129.
(42) Eriksson, T.; Hjelm, A. K.; Lindbergh, G.; Gustafsson, T. Kinetic study of LiMn2O4 cathodes by in situ XRD with constant-current cycling and potential stepping. *J. Electrochem. Soc.* **2002**, *149* (9), A1164−A1170.
(43) Ariyoshi, K.; Mizutani, S.; Makino, T.; Yamadaz, Y. A Clue to High Rate Capability of Lithium-Ion Batteries Obtained by an

https://doi.org/10.1021/acscentsci.1c00878
ACS Cent. Sci. XXXX, XXX, XXX−XXX

Electrochemical Approach Using "Diluted" Electrode. *J. Electrochem. Soc.* **2018**, *165* (16), A3965−A3970.
(44) Wolfman, M.; Khawaja, S.; Cabana, J. Mapping and Metastability of Heterogeneity in LiMn2O4 Battery Electrodes with High Energy Density. *J. Electrochem. Soc.* **2020**, *167* (2), 9.
(45) Kerlau, M.; Marcinek, M.; Srinivasan, V.; Kostecki, R. M. Studies of local degradation phenomena in composite cathodes for lithium-ion batteries. *Electrochim. Acta* **2007**, *52* (17), 5422−5429.
(46) Sun, K.; Zhao, C. H.; Lin, C. H.; Stavitski, E.; Williams, G. J.; Bai, J. M.; Dooryhee, E.; Attenkofer, K.; Thieme, J.; Chen-Wiegart, Y. C. K.; Gan, H. Operando Multi-modal Synchrotron Investigation for Structural and Chemical Evolution of Cupric Sulfide (CuS) Additive in Li-S battery. *Sci. Rep.* **2017**, *7*, 10.
(47) Wang, J. J.; Chen-Wiegart, Y. C. K.; Eng, C.; Shen, Q.; Wang, J. Visualization of anisotropic-isotropic phase transformation dynamics in battery electrode particles. *Nat. Commun.* **2016**, *7*, 1 DOI: 10.1038/ncomms12372.
(48) Xu, Y. H.; Hu, E. Y.; Zhan, K.; Wang, X. L.; Borzenets, V.; Sun, Z. H.; Pianetta, P.; Yu, X. Q.; Liu, Y. J.; Yang, X. Q.; Li, H. In situ Visualization of State-of-Charge Heterogeneity within a LiCoO2 Particle that Evolves upon Cycling at Different Rates. *Acs Energy Letters* **2017**, *2* (5), 1240−1245.
(49) Zhao, C. H.; Wada, T.; De Andrade, V.; Gursoy, D.; Kato, H.; Chen-Wiegart, Y. C. K. Imaging of 3D morphological evolution of nanoporous silicon anode in lithium ion battery by X-ray nano-tomography. *Nano Energy* **2018**, *52*, 381−390.
(50) Zhang, Q.; Brady, A. B.; Pelliccione, C. J.; Bock, D. C.; Bruck, A. M.; Li, J.; Sarbada, V.; Hull, R.; Stach, E. A.; Takeuchi, K. J.; Takeuchi, E. S.; Liu, P.; Marschilok, A. C. Investigation of Structural Evolution of Li1.1V3O8 by In Situ X-ray Diffraction and Density Functional Theory Calculations. *Chem. Mater.* **2017**, *29* (5), 2364−2373.
(51) Xia, H.; Luo, Z. T.; Xie, J. P. Nanostructured LiMn2O4 and their composites as high-performance cathodes for lithium-ion batteries. *Prog. Nat. Sci.* **2012**, *22* (6), 572−584.
(52) Ohzuku, T.; Kitagawa, M.; Hirai, T. Electrochemistry of Manganese-Dioxide in Lithium Nonaqueous Cell. 3. X-Ray Diffractional Study on the Reduction of Spinel-Related Manganese-Dioxide. *J. Electrochem. Soc.* **1990**, *137* (3), 769−775.
(53) Liu, W.; Kowal, K.; Farrington, G. C. Mechanism of the electrochemical insertion of lithium into LiMn2O4 spinels. *J. Electrochem. Soc.* **1998**, *145* (2), 459−465.
(54) Yang, X. Q.; Sun, X.; Lee, S. J.; McBreen, J.; Mukerjee, S.; Daroux, M. L.; Xing, X. K. In situ synchrotron X-ray diffraction studies of the phase transitions in LixMn2O4 cathode materials. *Electrochem. Solid-State Lett.* **1999**, *2* (4), 157−160.
(55) Bianchini, M.; Suard, E.; Croguennec, L.; Masquelier, C. Li-Rich Li1+xMn2-xO4 Spinel Electrode Materials: An Operando Neutron Diffraction Study during Li+ Extraction/Insertion. *J. Phys. Chem. C* **2014**, *118* (45), 25947−25955.
(56) Okumura, T.; Yamaguchi, Y.; Shikano, M.; Kobayashi, H. Further findings of X-ray absorption near-edge structure in lithium manganese spinel oxide using first-principles calculations. *J. Mater. Chem. A* **2014**, *2* (21), 8017−8025.
(57) Baumung, M.; Kollenbach, L.; Xi, L. F.; Risch, M. Undesired Bulk Oxidation of LiMn2O4 Increases Overpotential of Electrocatalytic Water Oxidation in Lithium Hydroxide Electrolytes. *ChemPhysChem* **2019**, *20* (22), 2981−2988.
(58) Lee, D. D.; Seung, H. S. Learning the parts of objects by non-negative matrix factorization. *Nature* **1999**, *401* (6755), 788−791.
(59) Fu, X.; Huang, K.; Sidiropoulos, N. D.; Ma, W. K. Nonnegative Matrix Factorization for Signal and Data Analytics: Identifiability, Algorithms, and Applications. *IEEE Signal Processing Magazine* **2019**, *36* (2), 59−80.

https://doi.org/10.1021/acscentsci.1c00878
ACS Cent. Sci. XXXX, XXX, XXX−XXX